



HAL
open science

Cluster magnification and the mass-richness relation in CFHTLenS

Jes Ford, Hendrik Hildebrandt, Ludovic van Waerbeke, Thomas Erben,
Clotilde Laigle, Martha Milkeraitis, Christopher B. Morrison

► **To cite this version:**

Jes Ford, Hendrik Hildebrandt, Ludovic van Waerbeke, Thomas Erben, Clotilde Laigle, et al.. Cluster magnification and the mass-richness relation in CFHTLenS. Monthly Notices of the Royal Astronomical Society, 2014, 439, pp.3755-3764. 10.1093/mnras/stu225 . insu-03645667

HAL Id: insu-03645667

<https://insu.hal.science/insu-03645667>

Submitted on 25 Apr 2022

HAL is a multi-disciplinary open access archive for the deposit and dissemination of scientific research documents, whether they are published or not. The documents may come from teaching and research institutions in France or abroad, or from public or private research centers.

L'archive ouverte pluridisciplinaire **HAL**, est destinée au dépôt et à la diffusion de documents scientifiques de niveau recherche, publiés ou non, émanant des établissements d'enseignement et de recherche français ou étrangers, des laboratoires publics ou privés.

Cluster magnification and the mass–richness relation in CFHTLenS

Jes Ford,¹★ Hendrik Hildebrandt,^{1,2} Ludovic Van Waerbeke,¹ Thomas Erben,²
Clotilde Laigle,^{1,3,4} Martha Milkeraitis¹ and Christopher B. Morrison²

¹Department of Physics and Astronomy, University of British Columbia, 6224 Agricultural Road, Vancouver, B.C. V6T 1Z1, Canada

²Argelander-Institut für Astronomie, Auf dem Hügel 71, D-53121 Bonn, Germany

³Institut d'Astrophysique de Paris & UPMC (UMR 7095), 98 bis boulevard Arago, F-75014 Paris, France

⁴Ecole polytechnique, F-91128 Palaiseau Cedex, France

Accepted 2014 January 31. Received 2014 January 29; in original form 2013 October 8

ABSTRACT

Gravitational lensing magnification is measured with a significance of 9.7σ on a large sample of galaxy clusters in the Canada–France–Hawaii Telescope Lensing Survey (CFHTLenS). This survey covers $\sim 154 \text{ deg}^2$ and contains over 18 000 cluster candidates at redshifts $0.2 \leq z \leq 0.9$, detected using the 3D-Matched Filter cluster-finder of Milkeraitis et al. We fit composite-NFW models to the ensemble, accounting for cluster miscentring, source-lens redshift overlap, as well as nearby structure (the two-halo term), and recover mass estimates of the cluster dark matter haloes in range of $\sim 10^{13} M_{\odot}$ to $2 \times 10^{14} M_{\odot}$. Cluster richness is measured for the entire sample, and we bin the clusters according to both richness and redshift. A mass–richness relation $M_{200} = M_0(N_{200}/20)^{\beta}$ is fit to the measurements. For two different cluster miscentring models, we find consistent results for the normalization and slope, $M_0 = (2.3 \pm 0.2) \times 10^{13} M_{\odot}$, $\beta = 1.4 \pm 0.1$ and $M_0 = (2.2 \pm 0.2) \times 10^{13} M_{\odot}$, $\beta = 1.5 \pm 0.1$. We find that accounting for the full redshift distribution of lenses and sources is important, since any overlap can have an impact on mass estimates inferred from flux magnification.

Key words: gravitational lensing; weak – galaxies; clusters; general – galaxies; photometry – dark matter.

1 INTRODUCTION

Clusters of galaxies are the most massive gravitationally bound structures in the Universe today. As such they can be useful cosmological probes, as well as laboratories for all kinds of interesting physics including galaxy evolution, star formation rates, and interactions of the intergalactic medium. There are several methods commonly used to estimate cluster masses (e.g. mass-to-light ratios, X-ray luminosities, the Sunyaev–Zeldovich effect), but among them gravitational lensing is unique in being sensitive to all mass along the line of sight, irrespective of its type or dynamical state (Bartelmann & Schneider 2001).

There are multiple ways to measure the signature of gravitational lensing, and each has its own specific advantages and limitations. Observation of strong lensing arcs and multiple images is extremely useful for studying the innermost regions of clusters, and getting precise mass estimates, but can only be applied to very massive objects which are observationally limited in number. On the other hand, weak lensing shear, which measures slight deformations in background galaxy shapes, can be applied across a much wider range of lens masses. Shear studies have been used with much

success to map large-scale mass distributions in the nearby universe (Massey et al. 2007; Van Waerbeke et al. 2013). However, because they rely on precise shape measurements, shear faces the practical limitation of an inability to sufficiently resolve sources for lenses more distant than a redshift of about 1 (Van Waerbeke et al. 2010).

A third approach to measuring gravitational lensing is through the magnification of background sources, observable either through source size and flux variations (Huff & Graves 2014; Schmidt et al. 2012), or the resultant modification of source number densities (Scranton et al. 2005; Hildebrandt, van Waerbeke & Erben 2009b; Hildebrandt et al. 2011, 2013; Ford et al. 2012; Morrison et al. 2012). Magnification has been recently measured using quasar variability as well (Bauer et al. 2011). Although relative to the shear, magnification will tend to have a lower signal-to-noise for typical low-redshift lenses, the requirement for source resolution is completely removed. This makes magnification competitive for higher redshift lenses, and especially for ground-based surveys where atmospheric seeing has a strong influence on image quality.

In this work, we adopt the number density approach, known as flux magnification, using Lyman-break galaxies (LBGs) for the lensed background sources. The observed number density of LBGs is altered by the presence of foreground structure, due to the apparent stretching of sky solid angle, and the consequential amplification of source flux. Because of the variation in slope of the LBG luminosity

★E-mail: jesford@phas.ubc.ca

function, magnification can either increase or decrease the number densities of LBGs, depending on their intrinsic magnitudes. By stacking many clusters we can overcome the predominant source of noise – physical source clustering (Hildebrandt et al. 2011).

In Section 2, we describe the cluster and background galaxy samples. Section 3 lays out the methodology for the measurement and modelling of the magnification signal. We discuss our results in Section 4 and conclude in Section 5. Throughout this paper, we give all distances in physical units, and use a standard Λ cold dark matter cosmology with $H_0 = 70 \text{ km s}^{-1} \text{ Mpc}^{-1}$, $\Omega_M = 0.3$, and $\Omega_\Lambda = 1 - \Omega_M = 0.7$.

2 DATA

For the magnification results presented in this paper, we are fortunate to work with a very large sample of galaxy cluster candidates and background galaxies in the Canada–France–Hawaii–Telescope Lensing Survey (CFHTLenS;¹ Erben et al. 2013; Hildebrandt et al. 2012). CFHTLenS is based on the Wide portion of the CFHTLenS, with deep five band photometry. The survey is composed of four separate fields, in turn divided into 171 individual pointings, covering a total of 154 deg^2 .

2.1 3D-MF Galaxy clusters

The 3D-Matched-Filter (3D-MF) cluster finding algorithm of Milkeraitis et al. (2010), essentially creates likelihood maps of the sky (in discrete redshift bins) and searches for peaks of significance above the galaxy background. The likelihood is estimated assuming that clusters follow a radial Hubble profile as well as a Schechter luminosity function. A significance peak of $>3.5\sigma$ is considered a cluster detection, since this reduces below 1 per cent the probability of Gaussian random noise fluctuations mimicking a true cluster. The reader is referred to Milkeraitis et al. (2010) for the details of the 3D-MF algorithm; here, we discuss only the essential points relevant to our purposes.

The radial component of the 3D-MF likelihood employs a cutoff radius of 1 Mpc, which was chosen to roughly correspond to the radius r_{200} of an $M_{200} \sim 3 \times 10^{13} M_\odot$ cluster. Milkeraitis et al. (2010) motivate this choice by the desire to optimally search for relatively high-mass clusters, but note that this radius will be less ideal for low-mass clusters. One should expect that random galaxy interlopers may contaminate the estimation of significance for likelihood peaks corresponding to lower mass clusters. This may be a key factor in explaining the wide range of cluster significances conferred upon low-mass clusters from simulations, while high-mass simulated clusters were assigned significances that correlated strongly with mass (see fig. 10 in Milkeraitis et al. 2010). Because peak significance may therefore not be an ideal mass proxy to use for the full cluster ensemble, in this work we rely upon a measure of the cluster richness, which is discussed in Section 2.1.2 below. Using cluster richness has the added benefit that the mass–richness relation can be measured and used as a scaling relation.

Using the 3D-MF method, a total of 18 036 galaxy cluster candidates (hereafter clusters) have been detected in CFHTLenS, at a significance of $>3.5\sigma$ above the background. In contrast to previous cluster magnification studies, which have been limited by small number statistics, this huge sample of clusters allows us to

pursue multiple avenues of investigation. In particular, we bin the clusters according to both richness and redshift, to recover trends in physical characteristics such as the mass–richness relation, and also investigate halo miscentring as a function of these parameters.

2.1.1 Cluster centres

Due to the nature of the method, the defined centres of the 3D-MF clusters, which are located at peaks in the likelihood map, do not necessarily coincide with member galaxies. Hence, the defined centres are notably different from many other cluster finders, which commonly choose the brightest cluster galaxy (BCG), the peak in X-ray emission, some type of (possibly luminosity-weighted) average of galaxy positions, or a combination of these, as a measure of the centre of a dark matter halo.

The choice of cluster centre is always ambiguous, both observationally and in simulations. One wants to know the centre of the dark matter distribution, as the point around which to measure a radially dependent signal. Obviously the dark matter cannot be directly seen, so an observable such as galaxies or X-ray emission must be used (see George et al. 2012 for an excellent review and analysis of cluster centroiding). The chosen centre of the cluster can be wrong for several reasons. The observable chosen (e.g. the BCG) may simply be offset from the true centre of the dark matter potential. Misidentification of the BCG can be a significant problem for this particular example as well (Johnston et al. 2007).

Perhaps a more interesting source for miscentring comes from the fact that clusters haloes are not perfectly spherical, and exhibit substructure and irregularities caused by their own unique mass assembly histories. Especially for very massive haloes, which have formed more recently and in many cases are still undergoing mergers and have yet to virialize, we really should not expect a clear centre to exist. Following visual inspection, Mandelbaum, Seljak & Hirata (2008) chose to exclude the most massive clusters from their weak lensing analysis for this very reason. Instead of throwing away the highest mass haloes in our sample, we include them in this study, but take care to account for possible miscentring effects.

Milkeraitis et al. (2010) tested for centroid offsets in 3D-MF by running the cluster-finder on simulations and comparing detected cluster centres to known centres. The simulations used were the mock catalogues of Kitzbichler & White (2007), which were created from a semi-analytic galaxy catalogue (De Lucia & Blaizot 2007) derived from the Millennium Simulation (Springel et al. 2005). Fig. 13 of that work shows the number of clusters detected as a function of distance from true cluster centre. Because 3D-MF was optimized to produce cluster catalogues that are as complete as possible (in contrast to, e.g. Gillis & Hudson 2011, which is designed to maximize purity), the trade-off is the presence of some contamination with false detections, especially at the low-mass end.

We use the numbers of clusters at each offset, and the contamination from Milkeraitis et al. (2010), to estimate the probability of radial offsets $P(R_{\text{offset}})$. We fit the result for each mass bin with a two-dimensional Gaussian distribution:

$$P(R_{\text{offset}}) = \frac{R_{\text{offset}}}{\sigma_{\text{offset}}^2} \exp \left[-\frac{1}{2} \left(\frac{R_{\text{offset}}}{\sigma_{\text{offset}}} \right)^2 \right]. \quad (1)$$

These resulting curves are presented in Fig. 1 (colours are selected to match those in fig. 13 of Milkeraitis et al. 2010), and for clarity we only show the data points for the bin that combines all clusters. We find consistent fits for the separate mass bins, which we list in

¹ www.cfhtlens.org; Data products available at <http://www.cadc-ccda.hia-ihh.nrc-cnrc.gc.ca/community/CFHTLenS/query.html>

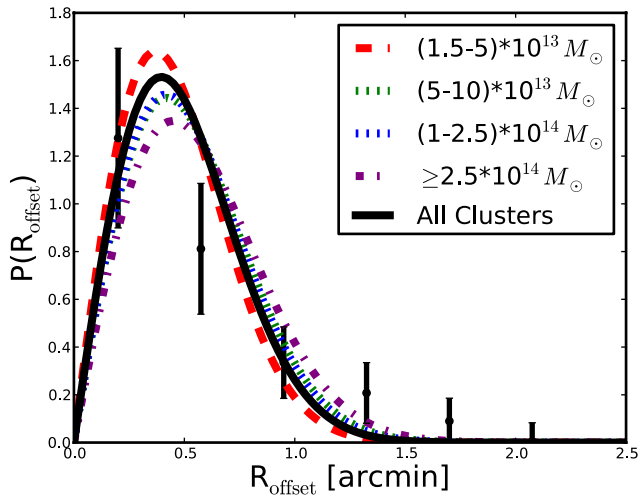


Figure 1. Modelled Gaussian distribution of radial offsets between defined 3DMF centres and simulated cluster centres. The black points and solid curve is the combined data and best fit for all CFHTLenS clusters combined. The coloured curves show the best-fitting Gaussians for separate mass bins, and colours match the empirical offsets measured and presented in fig. 13 of Milkeraitis et al. (2010). As each of these coloured curve fits is consistent with the solid black curve for the entire combined sample, we choose to use this single Gaussian distribution to model miscentring for all clusters.

Table 1. Best-fitting Gaussian distributions for the cluster miscentring in Fig. 1.

Mass range (M_{\odot})	Colour	Best-fitting σ_{offset} (arcmin)	χ_{red}^2
$(1.5-5) \times 10^{13}$	red	0.37 ± 0.06	1.8
$(5-10) \times 10^{13}$	green	0.42 ± 0.06	1.4
$(1-2.5) \times 10^{14}$	blue	0.42 ± 0.06	1.2
$\geq 2.5 \times 10^{14}$	purple	0.45 ± 0.06	1.4
$\geq 1.5 \times 10^{13}$	black	0.40 ± 0.06	1.1

Table 1, and therefore use the combined distribution (black curve) to model the effects of miscentring in our measurements.

2.1.2 Cluster richness

We define the richness parameter N_{200} in this work to be the number of galaxies within a radius r_{200} , and redshift Δz , of a cluster candidate centre (both points discussed below). Member galaxies are also required to be brighter than i -band absolute magnitude -19.35 . This cutoff is chosen to correspond to the limiting *apparent* magnitude of CFHTLenS ($i \sim 24$) at the highest redshift clusters that we probe, $z \sim 1$. So at the expense of removing many galaxies from the richness count, we hope to largely avoid the effect of incompleteness on the number of galaxies per cluster. Then clusters of the same intrinsic richness at high and low redshift should have comparable observed N_{200} , within the expected scatter of the mass–richness relation.

For the line-of-sight dimension, we require galaxies to fall within $\Delta z < 0.08(1+z)$ of the cluster redshift. This Δz is the 2σ scatter of photometric redshifts in the CFHTLenS catalogue, chosen so that we reduce the probability of galaxies in a cluster being missed due to errors in their photo- z estimation. Of course, this comes at the expense of counting galaxies within a quite broad line-of-sight extent, especially for the higher redshift clusters. This effect should cancel out though, since we also use the same Δz range in

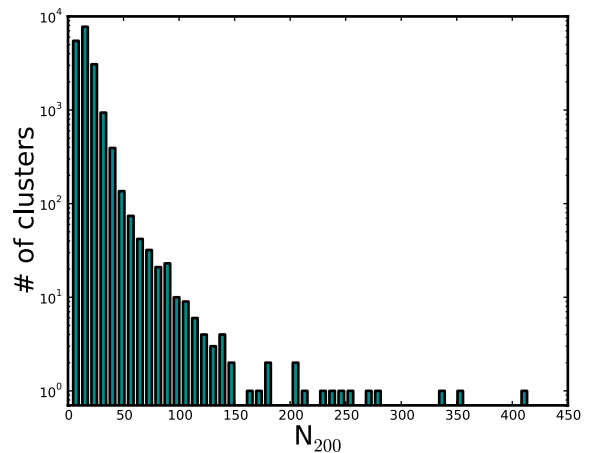


Figure 2. Distribution of richness (N_{200}) values for clusters in this study.

calculating the galaxy background density, which is subtracted to yield N_{200} as an overdensity count of cluster galaxy members.

In the plane of the sky, galaxies must lie within a projected radius r_{200} of the cluster centre (defined above). r_{200} is defined as the radius within which the average density is 200 times the critical energy density of the universe, $\rho_{\text{crit}}(z)$, evaluated at the redshift of the cluster. However, since r_{200} itself is unknown, we require some kind of assumption about radius or mass in order to proceed with the galaxy counting. There is no unique way to do this. We begin by making an initial approximation of the masses using a best-fitting power-law relation between mass and cluster peak significance, for 3D-MF clusters (Milkeraitis 2011):

$$\log(M_{200}) = 0.124\sigma + \log(10^{14} M_{\odot}) - 1.507. \quad (2)$$

As discussed in 2.1, 3D-MF tests on simulations that suggested peak significance was a good mass proxy for high, but not low, mass clusters. In light of this, we merely employ the above relation as a starting point for calculating the radii from mass,

$$r_{200} = \left[\frac{3M_{200}}{4\pi(200)\rho_{\text{crit}}(z)} \right]^{1/3}. \quad (3)$$

These r_{200} estimates are then used for counting galaxies for cluster richness. Richness N_{200} is the variable of choice used as a mass proxy for binning the magnification measurement. The distribution of these richness values is shown in Fig. 2.

2.2 Sources

We use LBGs as the magnified background sources. LBGs are high-redshift star-forming galaxies (Steidel et al. 1998), that have been successfully employed in past magnification studies (see Hildebrandt et al. 2009b, 2011; Ford et al. 2012; Morrison et al. 2012) due to the fact that their redshift distributions and luminosity functions are reasonably well understood. Knowledge of the intrinsic source luminosity function allows for an interpretation of the magnification signal, which depends sensitively on the slope of the number counts as a function of magnitude. In addition, the high-redshift nature of LBGs is important to reduce redshift overlap between lenses and sources. Any source galaxies in the redshift range of the cluster lenses will contaminate the lensing-induced cross-correlation signal, with correlations due to physical clustering.

The LBG sample is selected with the colour selection criteria of Hildebrandt et al. (2009a) (see section 3.2 of that paper). It is

composed of 122 144 u -dropouts with $23 < r \leq 24.5$, located at redshift ~ 3.1 . We choose this magnitude range to avoid as much potential low-redshift contamination as possible. See Section 3.2.2 for our modelling of the residual contamination. The detailed properties of this LBG population will be described in a forthcoming paper (Hildebrandt et al. in preparation).

3 MAGNIFICATION METHODOLOGY

3.1 The measurement

The magnification factor, μ , of a gravitational lens can be expressed in terms of the change from intrinsic (n_0) to observed (n) differential number counts of background sources:

$$n(m) dm = \mu^{\alpha-1} n_0(m) dm \quad (4)$$

(Narayan 1989). Here, m is apparent magnitude, and $\alpha \equiv \alpha(m)$ is proportional to the logarithmic slope of the source luminosity function. Depending on the luminosity function's slope in a given magnitude bin, it is possible to observe either an increase or a decrease in source number counts, as demonstrated in fig. 2 of Ford et al. (2012).

In practice, the magnification signal is easily measured using the optimally weighted cross-correlation function of Ménard et al. (2003):

$$w_{\text{opt}}(R) = \frac{S^{\alpha-1}L - S^{\alpha-1}R - (\alpha-1)LR}{RR} + (\alpha-1). \quad (5)$$

In this expression, the terms are normalized pair counts in radial bins, where L stands for the lenses, and $S^{\alpha-1}$ are the optimally weighted sources. R represents objects from a random catalogue more than 10 times the size of the source catalogue, with the same masks applied.

In order to determine the optimal weight factor $\alpha - 1$, for both the measurement and the interpretation, we require knowledge of the source luminosity function. As done in Ford et al. (2012), we determine the LBG luminosity function slope from the Schechter Function (Schechter 1976), giving

$$\alpha = 2.5 \frac{d}{dm} \log n_0(m) = 10^{0.4(M^* - M)} - \alpha_{\text{LF}} - 1, \quad (6)$$

and rely on externally measured luminosity functions for the characteristic magnitude M^* and faint end slope α_{LF} . We use the LBG luminosity function of van der Burg, Hildebrandt & Erben (2010), measured using much deeper data from the CFHTLS Deep fields. For u -dropouts M^* is -20.84 and α_{LF} is -1.6 . Thus, every source galaxy is assigned a weight factor of $\alpha - 1$ according to its absolute magnitude M .

The magnification signal, $w_{\text{opt}}(R)$, is measured in logarithmic radial bins of physical range 0.09–4 Mpc (in contrast to angle), so that we can stack clusters at different redshifts without mixing very different physical scales. Each cluster's signal is measured separately before stacking the measured $w_{\text{opt}}(R)$, and full covariance matrices are estimated from the different measurements.

3.2 The modelling

The magnification is a function of the halo masses, and to first order it is proportional to the convergence κ . In this work, however, we

will use the full expression for μ to account for any deviations from weak lensing in the inner regions of the clusters:

$$\mu = \frac{1}{(1 - \kappa)^2 - |\gamma|^2} \quad (7)$$

(Bartelmann & Schneider 2001).

We assume a spherical Navarro–Frenk–White (NFW) model (Navarro, Frenk & White 1997) for the dark matter haloes, along with the mass–concentration relation of Prada et al. (2012). The convergence is modelled as the sum of three terms,

$$\kappa = [p_{\text{cc}} \Sigma_{\text{NFW}} + (1 - p_{\text{cc}}) \Sigma_{\text{NFW}}^{\text{smoothed}} + \Sigma_{2\text{halo}}] / \Sigma_{\text{crit}}, \quad (8)$$

where p_{cc} is the fraction of clusters correctly centred (i.e. with $R_{\text{offset}} = 0$), and $\Sigma_{\text{crit}}(z)$ is the critical surface mass density at the lens redshift. The expression for the shear, γ , is identical with $\kappa \rightarrow \gamma$, and $\Sigma \rightarrow \Delta \Sigma$. Note that the first term in Equation (8) is equivalent to adding a delta function to the miscentred distribution of Fig. 1, to represent clusters with perfectly identified centres. As discussed in Section 4, the fits do not give strong preference to miscentring in the measurement, but in future work (in particular with weak lensing shear) it will be useful to constrain the degree of miscentring using the data, instead of relying solely on simulations.

We assume both lenses and sources are located at known discrete redshifts. This is $z \sim 3.1$ for the LBGs. Since they are at very high redshift the effect of any small offsets from this has negligible effect on the angular diameter distance, the relevant distance measure for lensing. The clusters, on the other hand, have redshift uncertainties of 0.05 [due to the shifting redshift slices employed by 3D-MF (Milkeraitis et al. 2010)]. This translates into an uncertainty on the mass estimates ranging from less than a percent up to ~ 17 per cent (depending on cluster z), and is included in the reported mass estimates.

Σ_{NFW} is the standard surface mass density for a perfectly centred NFW halo, calculated using expressions for κ (and γ) in Wright & Brainerd (2000). $\Sigma_{\text{NFW}}^{\text{smoothed}}$ on the other hand, is the expected surface mass density measured for a miscentred NFW halo:

$$\Sigma_{\text{NFW}}^{\text{smoothed}}(R) = \int_0^\infty \Sigma_{\text{NFW}}(R|R_{\text{offset}}) P(R_{\text{offset}}) dR_{\text{offset}}. \quad (9)$$

The distribution of offsets $P(R_{\text{offset}})$ is given by equation (1), and the other factor in the integrand is

$$\Sigma_{\text{NFW}}(R|R_{\text{offset}}) = \frac{1}{2\pi} \int_0^{2\pi} \Sigma_{\text{NFW}}(R') d\theta, \quad (10)$$

where $R' = \sqrt{R^2 + R_{\text{offset}}^2 + 2RR_{\text{offset}} \cos \theta}$ (Yang et al. 2006).

The two-halo term $\Sigma_{2\text{halo}}$ accounts for the fact that the haloes we study do not live in isolation, but are clustered as all matter in the universe is. We account for neighbouring haloes following the prescription of Johnston et al. (2007):

$$\Sigma_{2\text{halo}}(R, z) = b_l(M_{200}, z) \Omega_M \sigma_8^2 D(z)^2 \Sigma_l(R, z) \quad (11)$$

$$\Sigma_l(R, z) = (1+z)^3 \rho_{\text{crit},0} \int_{-\infty}^{\infty} \xi \left((1+z) \sqrt{R^2 + y^2} \right) dy \quad (12)$$

$$\xi(r) = \frac{1}{2\pi^2} \int_0^\infty k^2 P(k) \frac{\sin kr}{kr} dk. \quad (13)$$

Here, small r is comoving distance, $D(z)$ is the growth factor, $P(k)$ is the linear matter power spectrum, and σ_8 is the amplitude of the power spectrum on scales of $8 h^{-1}$ Mpc. For the lens bias factor $b_l(M_{200}, z)$, we use equation 5 of Seljak & Warren (2004).

3.2.1 Composite-halo fits

The part of the optimal correlation function which is caused by gravitation lensing is related to the magnification contrast $\delta\mu \equiv \mu - 1$ through

$$w_{\text{lensing}}(R) = \frac{1}{N_{\text{lens}}} \sum_{i=1}^{N_{\text{lens}}} \langle (\alpha - 1)^2 \rangle_i \delta\mu(R, M_{200})_i. \quad (14)$$

Here the sum is over the number of lenses in a given stacked measurement, and $\langle (\alpha - 1)^2 \rangle_i$ refers to the average of the weight factor squared in the pointing of a given cluster.

We perform composite-halo fits using the above prescription, in which we allow for the fact that the clusters in a given measurement have a range of masses and redshifts. We do not fit a single average mass. Instead, we calculate $\delta\mu(R, M_{200})_i$ for each individual cluster using a scaling relation between mass and richness,

$$M_{200} = M_0 \left(\frac{N_{200}}{20} \right)^\beta. \quad (15)$$

The fit parameters are the normalization, M_0 , and (log-) slope, $\log \beta$, of the assumed power-law relation. From this we calculate the optimal correlation $w_{\text{opt}}(R)$ according to equation (14). The best-fitting relation is determined by minimizing χ^2 , which is calculated using the full covariance matrix. We apply the correction factor from Hartlap, Simon & Schneider (2007) to the inverse covariance matrix; this corrects for a known bias (related to the number of data sets and bins) which would otherwise lead to our error bars being too small.

3.2.2 LBG contamination

An important source of systematic error for magnification comes from low-redshift contamination of the sources, leading to physical clustering between the lens and source populations. The cross-correlation that results from contamination can easily overwhelm the measurement of magnification, making redshift overlap far more important for magnification than for shear. Past studies sought to minimize this effect, for example by checking for the negative cross-correlation that should exist between lenses and very faint sources with shallow number count (Hildebrandt et al. 2009b; Ford et al. 2012). Here, we incorporate this clustering into the model, using a similar approach to Hildebrandt et al. (2013).

Fig. 3 shows the redshift probability distributions, $P(z)$, for the clusters and the LBGs. The LBG redshift distribution is based on the stacked posterior $P(z)$ put out by the BPZ redshift code (for details on the CFHTLenS photo- z see Hildebrandt et al. 2012). Since the BPZ prior is only calibrated for a magnitude-limited sample of galaxies, we cannot expect the stacked $P(z)$ to reflect the real redshift distribution of the colour-selected LBGs. Hence, we use

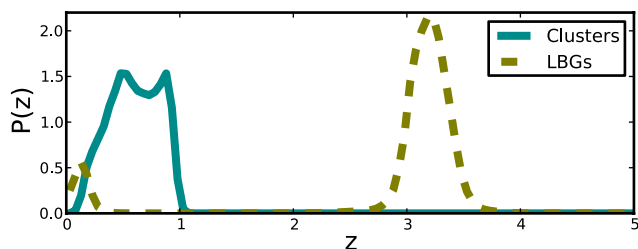


Figure 3. Redshift probability distribution functions for the clusters and the LBG sources. Low-redshift contamination of the LBGs will lead to physical clustering correlations where overlap with the cluster redshifts occurs.

the location and shape of the primary (high- z) and secondary (low- z) peaks but adjust their relative heights separately. This can be done with a cross-correlation technique similar to Newman (2008). Details of this technique will be presented in Hildebrandt et al. (in preparation).

Despite our efforts to avoid contamination, there is obviously some redshift overlap with the clusters. We use the products of the lens and source $P(z)$ to define selection functions, and calculate the expected angular correlations using the code from Hamana et al. (2004). The weighted correlation function that we measure is the sum of the correlations due to lensing magnification and clustering contamination:

$$w_{\text{opt}}(R, z) = f_{\text{lensing}} w_{\text{lensing}} + f_{\text{clustering}} w_{\text{clustering}}. \quad (16)$$

Note that $f_{\text{lensing}} + f_{\text{clustering}} \leq 1$, since some of the contaminants may be neither in the background and lensed, nor close enough in redshift to be clustered with the lenses.

The clustering contamination fraction $f_{\text{clustering}}(z)$ for each cluster redshift is defined as the fraction of each source $P(z)$ that lies within 0.1 in redshift (twice the cluster redshift uncertainty). The part of the source $P(z)$ that lies at higher redshift than the lens is then the lensed fraction $f_{\text{lensing}}(z)$, and the part at lower redshift (i.e. in front of the lens) has no contribution to the signal.

The factor $f_{\text{clustering}}(z)$ itself is generally very small for the LBGs used in this work, only really non-negligible for cluster redshifts $z \sim 0.2$ – 0.3 , which can be seen in Fig. 3. The more significant effect on the estimated masses is that $f_{\text{lensing}}(z) \sim 0.9$ across all redshift bins, because about 10 per cent of the sources are not really being lensed. We tested our results for robustness against uncertainties in the contamination fraction. When we vary the total low- z contamination fraction by $\pm 1\sigma$ (~ 4 per cent), the best-fitting cluster mass estimates remain within the stated error bars.

We explore three ways of determining $w_{\text{clustering}}$. Because of the weighting applied to LBGs in our measurement (which is optimal for the lensed sources, and should suppress contributions from redshift overlap), there will always be a prefactor of $\langle \alpha - 1 \rangle$ in each estimation of clustering. The first method uses the dark matter angular autocorrelation, w_{dm} , and estimates of the galaxy and cluster bias to calculate:

$$w_{\text{clustering}}(R, z) = \langle \alpha - 1 \rangle b_l b_s w_{\text{dm}}(R, z). \quad (17)$$

We set the bias factor for the galaxy contaminants $b_s = 1$ for this analysis, which is reasonably consistent with the bias relation of Seljak & Warren (2004) that is employed for the cluster bias (b_l).

We also calculate both the one- and two-halo terms for NFW haloes, $w_{1\text{halo}}$ and $w_{2\text{halo}}$ (again using the code and methods described in Hamana et al. 2004). Here, the expression for physical clustering takes the form:

$$w_{\text{clustering}}(R, z) = \langle \alpha - 1 \rangle b_s [w_{1\text{halo}}(R, z) + w_{2\text{halo}}(R, z)]. \quad (18)$$

This method requires knowledge of the occupation distribution of the low- z galaxy contaminants in the cluster dark matter haloes, which is not well determined. As a first approximation, we use the simple power-law form described in Hamana et al. (2004),

$$N_g(M) = \begin{cases} (M/M_1)^\alpha & \text{for } M > M_{\text{min}} \\ 0 & \text{for } M < M_{\text{min}} \end{cases}. \quad (19)$$

Since these parameters are unknown, we use the values for M_1 and α measured for galaxies in the SDSS (see table 3 of Zehavi et al. 2011). We choose M_{min} to correspond to the minimum mass measured for cluster haloes, and assume that haloes above this mass

always host a detected cluster. As a final check, we also ask what the clustering signal would be if every halo above M_{\min} hosted both a cluster and a single low- z galaxy contaminant (so that $N_g = 1$ for $M > M_{\min}$).

This final method yields the largest estimates of $w_{\text{clustering}}$, and therefore a smaller estimate of cluster masses. The former (using SDSS parameters) gives the highest mass estimates, and the simple biasing approach of equation (17) yields intermediate results. We use the range of these results to estimate an uncertainty in mass estimates coming from lack of knowledge about the nature of the low- z galaxies that contaminate our LBG source sample. This additional systematic error affects only the clusters at low redshift, where the source and lens $P(z)$ distributions overlap, and is reported on the mass estimates given in Table 3. All best-fitting mass values reported in the tables of this work are calculated using the contamination approach of equation (17), since this method relied on the fewest assumptions about the nature of the galaxy contaminants.

Accounting for redshift distributions in this particular source sample effectively means that cluster masses are *higher* than one would naively guess by fitting for only the magnification signal. However, note that in a case with more significant redshift overlap, so that $f_{\text{clustering}}$ was large, the opposite statement would be true, and mass estimates that included the full $P(z)$ distribution would be smaller than the naive magnification-only approach. These are important effects to consider, and future flux magnification studies should be careful to use full redshift distributions in modelling the measured signal.

4 RESULTS

Stacking the entire set of 18 036 clusters gives a total significance of 9.7σ for the combined detection, shown in Fig. 4. The perfectly centred model is a better fit to the overall measurement, with $\chi_{\text{red}}^2 \sim 1.2$, while the miscentred model gives χ_{red}^2 of 2.3. For both models, there are two free parameters (M_0 and $\log \beta$), leading to

8 degrees of freedom. To investigate miscentring and mass–richness scaling, we divide the clusters into six richness bins, and measure the optimal cross-correlation in each.

We measure the characteristic signature of magnification in every richness bin with significances between 4.6 and 5.9σ . These results are shown in Fig. 5, where we try fitting both a perfectly centred model ($p_{\text{cc}} = 1$) and a model where every cluster is affected by centroid offsets ($p_{\text{cc}} = 0$). Details of the fits, including reduced χ^2 and the average of the best-fitting mass values (M_{200}), are given in Table 2.

The lowest mass (richness) bin is not well fitted by either model. Overall there is not a strong preference for either perfectly centred ($p_{\text{cc}} = 1$) or miscentred ($p_{\text{cc}} = 0$) clusters, and both are reasonably good fits. Generally, the miscentred model yields slightly higher masses for the clusters (though it is sensitive to the shape of the data), due to the Gaussian smoothing applied, which lowers the model amplitude in the innermost regions. However, this is easily within the uncertainty on the mass estimates, so the results are in agreement.

The issue of cluster miscentring is interesting in its own right as discussed in Section 2.1.1. It is tempting to try and fit for the parameter p_{cc} , describing the fraction that are actually correctly centred, or else for the miscentring Gaussian width σ_{offset} , as done in Johnston et al. (2007). The issue here is a strong degeneracy between p_{cc} , σ_{offset} , and cluster concentration. Increasing the number of clusters that have offset centres produces essentially the same results as leaving p_{cc} fixed and increasing σ_{offset} , an effect that can be mimicked by a lower concentration in the NFW model. We run the risk of overfitting to the results.

In fact, Johnston et al. (2007) found very little constraining power on the miscentring width and the fraction of miscentred MaxBCG clusters, and applied strong priors to these distributions. George et al. (2012) performed an extensive weak lensing miscentring study of groups in the cosmological evolution survey (COSMOS), and chose to forgo the additional parameter p_{cc} ,

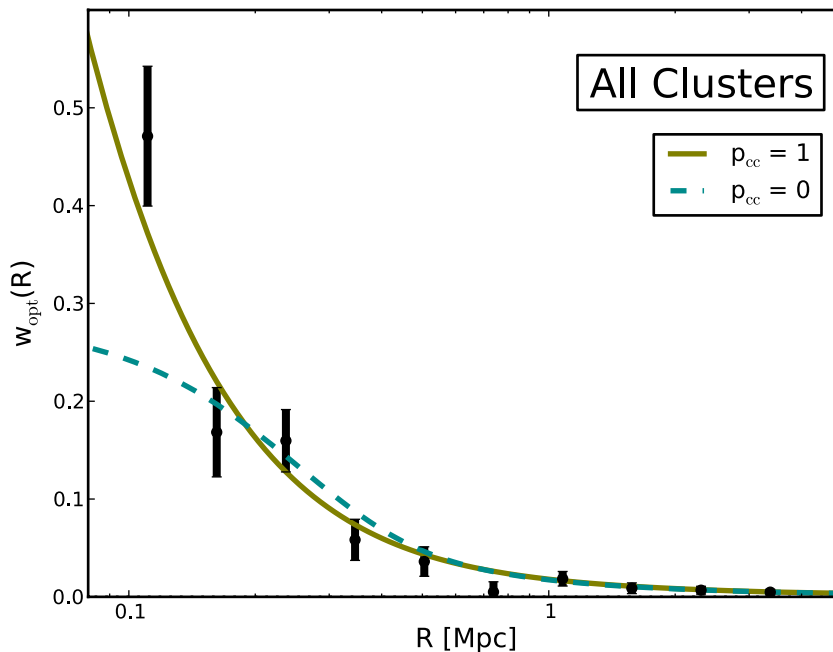


Figure 4. Optimal cross-correlation signal measured for the entire stacked sample of 18 024 clusters. The model fits are both composite-NFW (see the text for all terms in the fit). The solid line assumes that the clusters are perfectly centred on the peak likelihood of the 3DMF cluster detection, while the dashed line includes the effects of cluster miscentring.

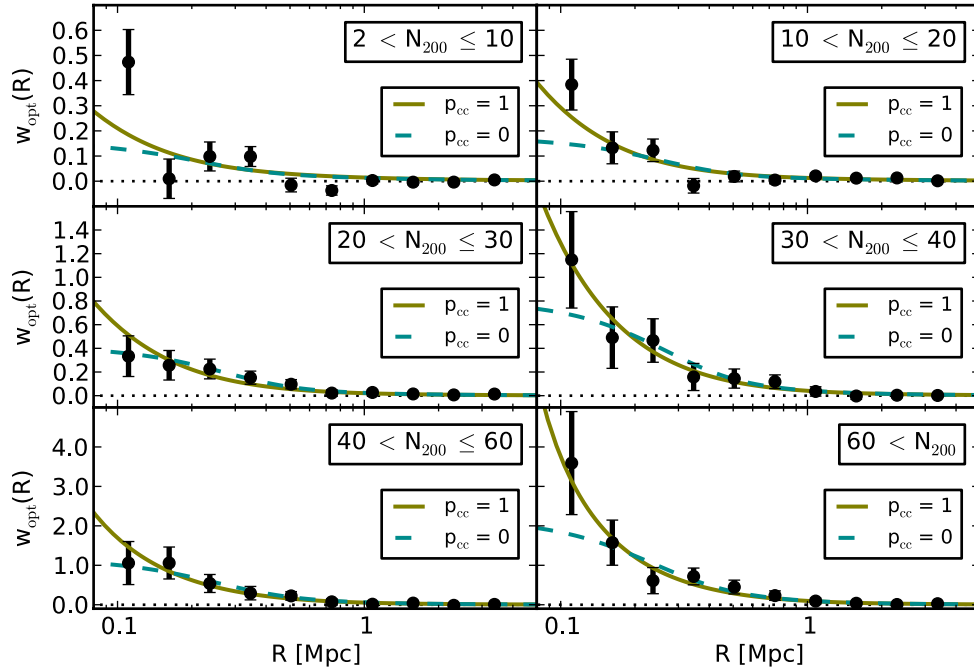


Figure 5. Optimal cross-correlation signal measured for each N_{200} (richness) bin. Two composite-NFW fits are shown. The solid curve assumes clusters are perfectly centred, while the dashed curve accounts for cluster miscentring, using the Gaussian offset distribution modelled in Fig. 1 and discussed in Section 3.2.

Table 2. Details of fits for richness-binned measurements in Fig. 5. We list the richness range selected, the number of clusters in that bin, the detection significance, the average richness of the bin, and the mass estimates and reduced χ^2 for both the centred and miscentred models fit to the data. Note that the average mass given is not the value fit itself, but the average of all resulting masses fit using the composite-halo approach discussed in Section 3.2.1.

Richness	No. of Clusters	Significance	$\langle N_{200} \rangle$	$p_{cc} = 1: \langle M_{200} \rangle$	χ^2_{red}	$p_{cc} = 0: \langle M_{200} \rangle$	χ^2_{red}
$2 < N_{200}$	18 036	9.7σ	17	$(2.0 \pm 0.3) \times 10^{13} M_{\odot}$	1.2	$(1.8 \pm 0.3) \times 10^{13} M_{\odot}$	2.3
$2 < N_{200} < 10$	4453	5.3σ	8	$(0.9 \pm 0.5) \times 10^{13} M_{\odot}$	3.0	$(0.7 \pm 0.4) \times 10^{13} M_{\odot}$	3.2
$10 < N_{200} < 20$	9398	5.9σ	15	$(1.3 \pm 0.3) \times 10^{13} M_{\odot}$	1.6	$(1.0 \pm 0.3) \times 10^{13} M_{\odot}$	2.2
$20 < N_{200} < 30$	2967	5.4σ	24	$(2.9 \pm 0.7) \times 10^{13} M_{\odot}$	0.7	$(3.3 \pm 0.8) \times 10^{13} M_{\odot}$	0.3
$30 < N_{200} < 40$	695	5.0σ	35	$(7 \pm 2) \times 10^{13} M_{\odot}$	0.3	$(7 \pm 2) \times 10^{13} M_{\odot}$	0.5
$40 < N_{200} < 60$	351	4.6σ	47	$(1.0 \pm 0.2) \times 10^{14} M_{\odot}$	0.4	$(1.1 \pm 0.2) \times 10^{14} M_{\odot}$	0.3
$60 < N_{200}$	172	5.5σ	99	$(2.0 \pm 0.4) \times 10^{14} M_{\odot}$	0.5	$(2.1 \pm 0.4) \times 10^{14} M_{\odot}$	0.6

as they achieved sufficiently good fits without it. Mandelbaum et al. (2008) performed a lensing analysis of the MaxBCG clusters, and found that including miscentring effects with the Johnston et al. (2007) prescription strongly affected the resultant fits for concentration, again asserting the degeneracies of these parameters. Mandelbaum et al. (2008) conclude that this method of accounting for miscentring depends heavily on the mock catalogues from which the input parameters are generated, and in the case of MaxBCG clusters likely overcompensates.

In a forthcoming paper, we will present weak lensing shear measurements of these clusters, as well as a more detailed investigation of the centroiding, as well as a more detailed investigation of the centroiding. Shear, being proportional to the differential surface mass density, is more affected by offset centres than magnification (Johnston et al. 2007), and will be a better probe of miscentring.

4.1 The mass–richness relation

We observe a prominent scaling of best-fitting mass to richness, across the six richness bins (although the first two bins do generally have overlapping error bars). We plot this trend in Fig. 6, showing the average of the fit masses as a function of average cluster richness

in each bin. Note that the distribution of N_{200} in a bin is not uniform, and in the case of the highest richness bin the distribution is highly skewed (see Fig. 2).

We fit a simple power-law, equation (15), to these points, using the same plotted colour and line schemes for perfectly centred and miscentred clusters. For this cluster sample, we find that the best fit gives the normalization and slope of the mass–richness relation to be

$$M_0 = (2.3 \pm 0.2) \times 10^{13} M_{\odot}, \quad \beta = 1.4 \pm 0.1 \quad (20)$$

for the perfectly centred $p_{cc} = 1$ case, and

$$M_0 = (2.2 \pm 0.2) \times 10^{13} M_{\odot}, \quad \beta = 1.5 \pm 0.1 \quad (21)$$

for the miscentred $p_{cc} = 0$ case. The reduced χ^2 are 0.9 and 1.7, respectively (4 degrees of freedom), and there is good agreement between the two different centring scenarios explored here.

It is difficult to directly compare the results for the mass–richness relation in this work to other studies. The main reason is that the richness N_{200} we use is different than other definitions, which often count only red-sequence galaxies. Some uncertainty exists in the measure of richness as well, which we do not include in the analysis. Alternative measures of cluster richness would yield different

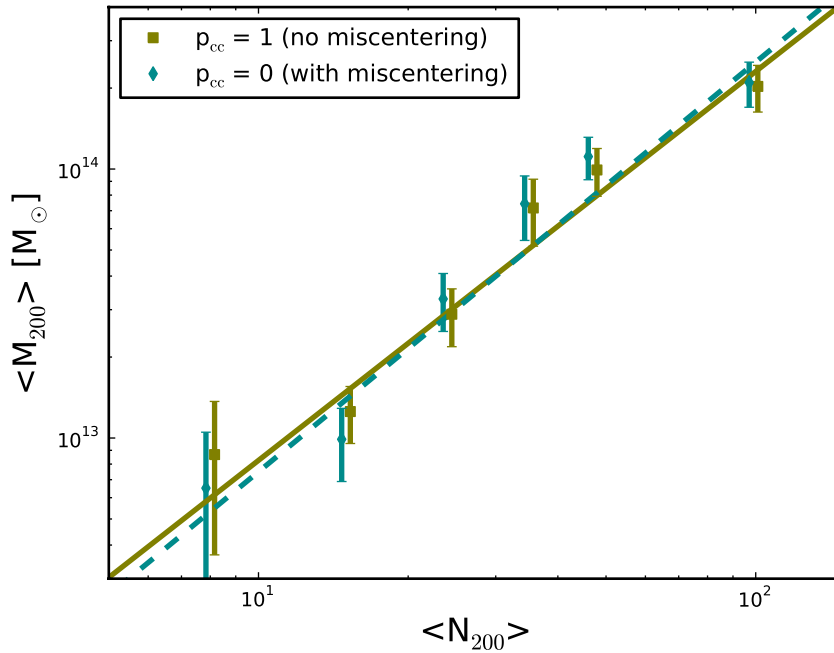


Figure 6. Cluster mass–richness relation, using the same N_{200} bins as in Fig. 5. Power-law fits to the data are presented for both cases of with (blue diamonds and dashed line) and without (green squares and solid line) the effects of miscentering. Points are slightly offset horizontally for clarity.

scaling relations. Another factor is the cluster sample, which was compiled using a novel cluster-finder, and may well have different characteristics than other samples in the literature. In a follow-up paper, we will present a shear analysis of the CFHTLenS clusters, and compare the mass–richness relation obtained using that complementary probe of halo mass.

4.2 Redshift binning

Finally, we investigate the magnification as a function of redshift. We stack clusters of all richnesses, at each redshift in the catalogue, $0.2 \leq z \leq 0.9$, and measure the optimal correlations in each. This is displayed in Fig. 8. We observe a steady decrease in measured signal as the cluster redshift increases from $z \sim 0.2$ to 0.5, then roughly consistent measurements from $0.6 \leq z \leq 0.8$, followed by rather low signal at $z \sim 0.9$.

The N_{200} distributions in Fig. 7 show that these trends cannot be caused by deviations in richness between these different cluster

redshifts. This is difficult to reconcile with the clear mass–richness scaling observed when all redshifts are combined. Table 3 shows that detection significance for each redshift bin is more tightly linked to mass than the $\langle N_{200} \rangle$. Perhaps the richness estimates used in this work are not optimized for use as a mass proxy at all redshifts. Another possibility is that we have not correctly accounted for redshift overlap between samples. If the contamination fraction is higher than estimated, this could lead to a boost in correlation strength at low redshift, as well as a depletion at higher redshift. However, it is still very difficult to explain the anomalously low measurement at intermediate redshift, $z \sim 0.5$, with this reasoning.

One factor that we have not accounted for is possible cluster false detections in our sample. Since 3D-MF was optimized to produce cluster catalogues that are as complete as possible, false detection rates could be quite high. In particular, we would expect these rates to increase at high redshift, which would also weaken those measured correlations. We note in particular that cluster redshift bins $z \sim 0.5$ and 0.9, which yield relatively low

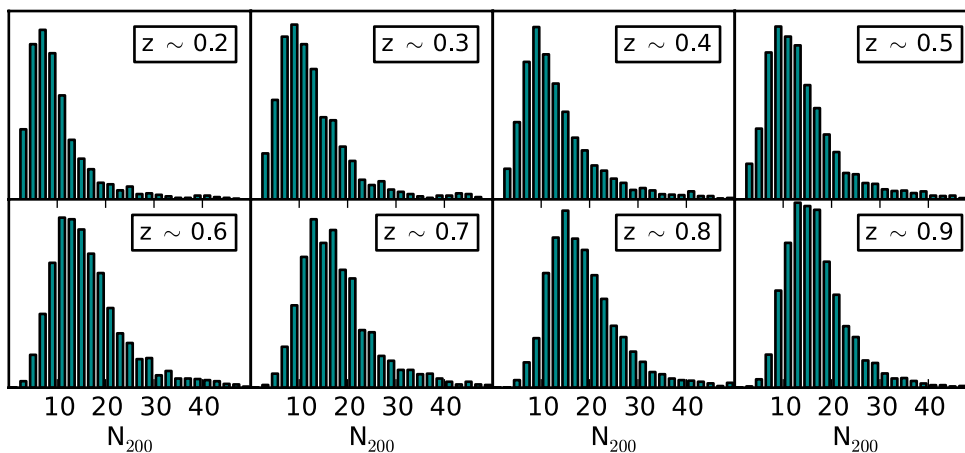


Figure 7. N_{200} distributions as a function of cluster redshift.

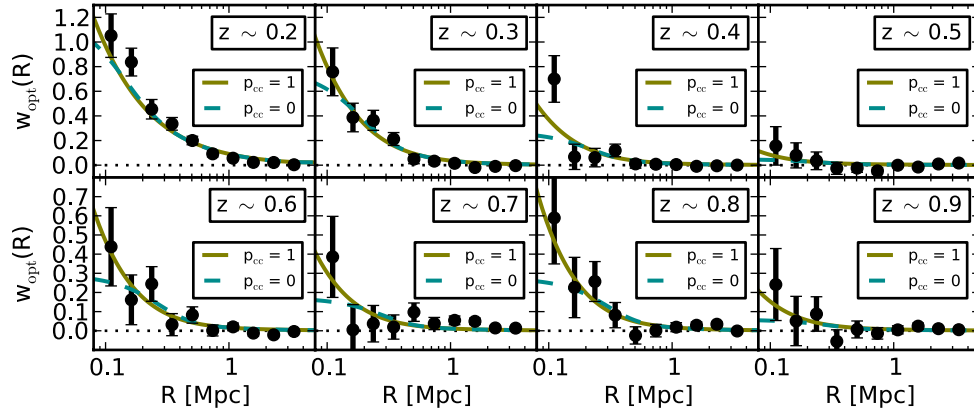


Figure 8. Optimal correlation for clusters binned in redshift.

Table 3. Details of fits for redshift-binned measurements in Fig. 8. We list the same bin properties and fits given in Table 2, as well as $f_{\text{clustering}}$, which is the total fraction of LBGs expected to lie within $\Delta z \sim 0.1$ of the cluster z .

Redshift	$f_{\text{clustering}}$	Clusters	Significance	$\langle N_{200} \rangle$	$p_{cc} = 1: \langle M_{200} \rangle$	χ^2_{red}	$p_{cc} = 0: \langle M_{200} \rangle$	χ^2_{red}
$z \sim 0.2$	0.07	1157	12.5σ	11.6	$(9 \pm 2 \pm 2^{\text{sys}}) \times 10^{13} M_{\odot}$	3.6	$(9 \pm 2 \pm 2^{\text{sys}}) \times 10^{13} M_{\odot}$	3.4
$z \sim 0.3$	0.02	1515	8.0σ	14.4	$(6 \pm 1 \pm 1^{\text{sys}}) \times 10^{13} M_{\odot}$	2.2	$(6 \pm 1 \pm 1^{\text{sys}}) \times 10^{13} M_{\odot}$	2.1
$z \sim 0.4$	3×10^{-3}	2242	4.6σ	15.2	$(1.9 \pm 0.7) \times 10^{13} M_{\odot}$	1.4	$(1.6 \pm 0.7) \times 10^{13} M_{\odot}$	1.6
$z \sim 0.5$	4×10^{-4}	2932	4.0σ	15.9	$(0.3 \pm 0.4) \times 10^{13} M_{\odot}$	1.9	$(0.2 \pm 0.5) \times 10^{13} M_{\odot}$	1.9
$z \sim 0.6$	1×10^{-4}	2455	4.6σ	18.0	$(2.2 \pm 0.8) \times 10^{13} M_{\odot}$	1.5	$(2.0 \pm 0.8) \times 10^{13} M_{\odot}$	1.6
$z \sim 0.7$	2×10^{-5}	2331	4.5σ	19.3	$(1.2 \pm 0.7) \times 10^{13} M_{\odot}$	1.7	$(1.1 \pm 0.7) \times 10^{13} M_{\odot}$	1.9
$z \sim 0.8$	2×10^{-5}	2364	4.9σ	19.9	$(2.5 \pm 0.9) \times 10^{13} M_{\odot}$	1.5	$(2.2 \pm 0.9) \times 10^{13} M_{\odot}$	1.7
$z \sim 0.9$	2×10^{-5}	3040	2.6σ	17.6	$(0.5 \pm 0.5) \times 10^{13} M_{\odot}$	0.6	$(0.3 \pm 0.6) \times 10^{13} M_{\odot}$	0.8

cluster masses, are seen in Fig. 3 to have excess numbers of detected clusters, possibly an indication of higher false detection rates at these redshifts.

5 CONCLUSIONS

We present the most significant magnification-only cluster measurement to date, at 9.7σ . A sample of 18 036 cluster candidates has been detected using the 3D-MF technique in the $\sim 154 \text{ deg}^2$ CFHTLenS survey. In this analysis, we have investigated the mass of cluster dark matter haloes, from flux magnification, as a function of both richness and redshift. A forthcoming paper will present the weak lensing shear analysis of these clusters as well.

We fit a composite-NFW model that accounts for the full redshift and mass ranges of the cluster sample, as well as redshift overlap with low- z source contaminants, cluster halo miscentring, and the two-halo term. We find that the entire cluster sample is marginally better fit by the model that does not include miscentring, but do not see a strong preference either way across richness bins. In the future, shear measurements, which are more sensitive to miscentring, may illuminate this aspect of the investigation.

We observe a strong scaling between measured mass and cluster richness, and fit a simple power-law relation to the data. The two miscentring models explored in this work yield consistent values for the normalization and slope of the mass–richness relation.

We have attempted to account for the contamination of our background sources with low- z galaxies. This is a serious systematic effect for magnification, as redshift overlap between lenses and sources will lead to physical clustering correlations, swamping the lensing-induced correlations that we want to measure. We use the full stacked redshift probability distributions for the lens and source

populations, and include the expected clustering contribution in our model. In spite of this we see unexpected features in the redshift-binned measurements. Part of the reason could come from cluster false detections, which can be high for the 3D-MF method which is optimized for completeness. Another contribution could come from errors in the source redshift distributions. Accounting for redshift overlap is imperative if significant overlap exists between the lens and source distributions, or else mass estimates can end up very biased.

This is the first analysis presented of the 3D-MF clusters in CFHTLenS, but much more science is left to do with the sample. In particular, a more thorough investigation of the miscentring problem will be carried out in the forthcoming shear analysis, where it will be possible to compare different candidate centres. Another interesting question is whether dust can be detected on cluster scales by simultaneously measuring the chromatic extinction along with flux magnification. Finally different background source samples may be employed to improve signal-to-noise, but only if their redshift distributions can be well determined. We leave these tasks to future work.

This work has been an important step in the development of weak lensing magnification measurements, and the progression from signal detection to science. Many upcoming surveys will benefit from the inclusion of magnification in their lensing programmes, as the technique offers a very complimentary probe of large-scale structure. Since measuring flux magnification is not a strong function of image quality, it is especially useful for ground-based surveys which must deal with atmospheric effects. Next generation surveys like the large synoptic survey telescope (LSST), the wide-field infrared survey telescope (WFIRST), and Euclid, will have greater numbers of sources, and improved redshift probability distribution

estimates, so we can expect future magnification studies to yield important contributions to weak lensing science and cosmology.

ACKNOWLEDGEMENTS

We thank the CFHTLenS team for making their catalogues publicly available to download from www.cfhtlens.org. This work is partly based on observations obtained with MegaPrime/MegaCam, a joint project of CFHT and CEA/IRFU, at the Canada–France–Hawaii Telescope (CFHT) which is operated by the National Research Council (NRC) of Canada, the Institut National des Sciences de l’Univers of the Centre National de la Recherche Scientifique (CNRS) of France, and the University of Hawaii. This research used the facilities of the Canadian Astronomy Data Centre operated by the National Research Council of Canada with the support of the Canadian Space Agency. CFHTLenS data processing was made possible thanks to significant computing support from the NSERC Research Tools and Instruments grant program.

JF is supported by a UBC Four-Year-Fellowship and NSERC. HH is supported by the Marie Curie IOF 252760, a CITA National Fellowship and the DFG grant Hi 1495/2-1. LVW is supported by NSERC and CIFAR.

Author Contributions: JF led the analysis, wrote all code for the magnification measurement and modelling, and prepared the draft of this paper. HH and LVW contributed very significantly to the overarching approach and detailed form of the analysis, through countless meetings, emails, and discussions. In addition, HH is responsible for producing the photometric redshifts and LBG catalogues used in this work. TE did all the CFHTLenS data reduction. CL wrote the first version of the code used for calculating cluster richness. MM developed the 3D-MF cluster finding algorithm which was used to produce the entire CFHTLenS cluster candidate sample. CM performed an analysis of LBG contamination to determine the fraction of sources at low redshift.

REFERENCES

Bartelmann M., Schneider P., 2001, *Phys. Rep.*, 340, 291
 Bauer A. H., Seitz S., Jerke J., Scalzo R., Rabinowitz D., Ellman N., Baltay C., 2011, *ApJ*, 732, 64
 De Lucia G., Blaizot J., 2007, *MNRAS*, 375, 2
 Erben T. et al., 2013, *MNRAS*, 433, 2545
 Ford J. et al., 2012, *ApJ*, 754, 143

George M. R. et al., 2012, *ApJ*, 757, 2
 Gillis B. R., Hudson M. J., 2011, *MNRAS*, 410, 13
 Hamana T., Ouchi M., Shimasaku K., Kayo I., Suto Y., 2004, *MNRAS*, 347, 813
 Hartlap J., Simon P., Schneider P., 2007, *A&A*, 464, 399
 Hildebrandt H., Pielorz J., Erben T., van Waerbeke L., Simon P., Capak P., 2009a, *A&A*, 498, 725
 Hildebrandt H., van Waerbeke L., Erben T., 2009b, *A&A*, 507, 683
 Hildebrandt H. et al., 2011, *ApJ*, 733, L30
 Hildebrandt H. et al., 2012, *MNRAS*, 421, 2355
 Hildebrandt H. et al., 2013, *MNRAS*, 429, 3230
 Huff E. M., Graves G. J., 2014, *ApJ*, 780, L16
 Johnston D. E. et al., 2007, preprint ([arXiv:0709.1159](https://arxiv.org/abs/0709.1159))
 Kitzbichler M. G., White S. D. M., 2007, *MNRAS*, 376, 2
 Mandelbaum R., Seljak U., Hirata C. M., 2008, *J. Cosmol. Astropart. Phys.*, 8, 6
 Massey R. et al., 2007, *Nature*, 445, 286
 Ménard B., Hamana T., Bartelmann M., Yoshida N., 2003, *A&A*, 403, 817
 Milkeraitis M., 2011, PhD thesis, Univ. British Columbia
 Milkeraitis M., van Waerbeke L., Heymans C., Hildebrandt H., Dietrich J. P., Erben T., 2010, *MNRAS*, 406, 673
 Morrison C. B., Scranton R., Ménard B., Schmidt S. J., Tyson J. A., Ryan R., Choi A., Wittman D. M., 2012, *MNRAS*, 426, 2489
 Narayan R., 1989, *ApJ*, 339, L53
 Navarro J. F., Frenk C. S., White S. D. M., 1997, *ApJ*, 490, 493
 Newman J. A., 2008, *ApJ*, 684, 88
 Prada F., Klypin A. A., Cuesta A. J., Betancort-Rijo J. E., Primack J., 2012, *MNRAS*, 423, 3018
 Schechter P., 1976, *ApJ*, 203, 297
 Schmidt F., Leauthaud A., Massey R., Rhodes J., George M. R., Koekemoer A. M., Finoguenov A., Tanaka M., 2012, *ApJ*, 744, L22
 Scranton R. et al., 2005, *ApJ*, 633, 589
 Seljak U., Warren M. S., 2004, *MNRAS*, 355, 129
 Springel V. et al., 2005, *Nature*, 435, 629
 Steidel C. C., Adelberger K. L., Dickinson M., Giavalisco M., Pettini M., 1998, preprint ([astro-ph/9812167](https://arxiv.org/abs/astro-ph/9812167))
 van der Burg R. F. J., Hildebrandt H., Erben T., 2010, *A&A*, 523, A74
 Van Waerbeke L., Hildebrandt H., Ford J., Milkeraitis M., 2010, *ApJ*, 723, L13
 Van Waerbeke L. et al., 2013, *MNRAS*, 433, 3373
 Wright C. O., Brainerd T. G., 2000, *ApJ*, 534, 34
 Yang X., Mo H. J., van den Bosch F. C., Jing Y. P., Weinmann S. M., Meneghetti M., 2006, *MNRAS*, 373, 1159
 Zehavi I. et al., 2011, *ApJ*, 736, 59

This paper has been typeset from a $\text{\TeX}/\text{\LaTeX}$ file prepared by the author.